

Shadow Images of Ghosh-Kumar Rotating Black Hole Illuminated By Spherical Light Sources and Thin Accretion Disks

Chen-Yu Yang,^{1,2,*} M. Israr Aslam,^{3,†} Xiao-Xiong Zeng,^{1,2,‡} and Rabia Saleem^{3,§}

¹*State Key Laboratory of Mountain Bridge and Tunnel Engineering,
Chongqing Jiaotong University, Chongqing 400074, China*

²*Department of Mechanics, Chongqing Jiaotong University, Chongqing 400074, China*

³*Department of Mathematics, COMSATS University Islamabad, Lahore Campus, Lahore-54000 Pakistan.*

(Dated: November 19, 2024)

This study investigates the astronomical implications of the Ghosh-Kumar rotating Black Hole (BH), particularly its behaviour on shadow images, illuminated by celestial light sources and equatorial thin accretion disks. Our research delineates a crucial correlation between dynamics of the shadow images and the parameters a , q and the θ_{obs} , which aptly reflect the influence of the model parameters on the optical features of shadow images. Initially, elevated behavior of both a and q transforms the geometry of the shadow images from perfect circles to an oval shape and converges them towards the centre of the screen. By imposing the backward ray-tracing method, we demonstrate the optical appearance of shadow images of the considering BH spacetime in the celestial light source. The results demonstrate that the Einstein ring shows a transition from an axisymmetric closed circle to an arc-like shape on the screen as well as producing the deformation on the shadow shape with the modifications of spacetime parameters at the fixed observational position. Next, we observe that the attributes of accretion disks along with the relevant parameters on the shadow images are illuminated by both prograde and retrograde accreting flow. Our study reveals the process by which the accretion disk transitions from a disk-like structure to a hat-like shape with the aid of observational angles. Moreover, with an increase of q , the observed flux of both direct and lensed images of the accretion disk gradually moves towards the lower zone of the screen. Furthermore, we present the intensity distribution of the redshift factors on the screen. Our analysis suggests that the observer can see both redshift and blueshift factors on the screen at higher observational angles, while augmenting the values of both a and q , enhancing the effect of redshift on the screen.

Keywords: Rotating Black Holes; Non-linear Electrodynamics; Shadows; AdS/CFT Correspondence.

I. INTRODUCTION

Black hole, which is regarded as one of the most incomprehensible compact objects in the universe, have received a huge amount of observational evidence to present. In 2019, the Event Horizon Telescope (EHT) has been instrumental in capturing the images of the super-massive BH at the heart of the galaxy Messier 87 (M87), based on 1.3 interferometric observations [1–6]. This is a substantial evidence of the presence of BHs, and it raises the compelling prospect of testing General Relativity (GR) in the future high resolution images of BHs. Moreover, EHT reported that the configuration of the magnetic field, surrounding the accretion disk, clarifying that the magnetically seized accretion disk is consistent with the predictions of general relativistic magnetohydrodynamic simulations models [7, 8]. Recently, EHT released the first horizon-scale high resolution image of the Sagittarius (Sgr A^*), which is positioned at the heart of the milky way and showed that the angular size of the photon ring of the Sgr A^* is consistent with the radius of the shadow critical curve, as calculated in GR within the range of 10% nicely [9–14]. Under the shadow of these discoveries, it is reasonable to hypothesize that the accretion disk surrounding the BH could be influencing the observational characteristics of the BH shadows.

Since observations are susceptible to astronomical environments around BHs, the intensity to which the current optical appearance of bright rings is enforced by the photon rings is still a debatable topic in the scientific community [15–17]. Hence, it is necessary to analyze the physical properties of astronomical environments and their contributions

*chenyu_yang2024@163.com

†mrisraraslam@gmail.com

‡xxzengphysics@163.com

§rabiasaleem@cuilahore.edu.pk

to the BH shadows in more detail. As it is well-known in literature, a supermassive BH surrounding a radiating plasma results in a luminous accretion disk. The thermal synchronised electrons are thought to be the primary source of light in BH image investigation. Moreover, in the case of a high rotating BH, the emitted radiation can induce a phenomenon, so-called a relativistic jet [18]. The jet's base is surrounded by the funnel wall, which can produce not only potentially triggers substantial amounts of thermal electromagnetic radiation, but also transforms the jet into a precise metamorphosis. In this scenario, the jet and accretion disc both contribute as essential background light sources that are vital to the BHs horizon-scale imaging procedures. It is widely acknowledged that in the surroundings of the rotating BHs, there prevails a photon region, which consists of orbits where photons move at a continuously constant radial distance, known as bound photon orbits. This photon region is also known as the photon sphere in the case of static BHs. When these orbits undergo a radial unstable perturbations, then the photons on contiguous orbits, that are not perfectly in the photon zone, may experience multiple half orbits around the bound orbit before either emerging or falling into the BH, are the so-called nearly confined bound photon orbits. And the photons that are close to the bound orbits manifest as an angular aspect on the observer screen, are almost near the critical curve, known as the photon ring [19–21].

The possible observational properties of the BHs shadows and their related consequences were investigated for a long time. In 1979, Lunin considered the radiation from a thin accretion disk surrounding the BH and obtained simulated images of a BH with thin accretion disk, which illustrates that the emergence of the BH shadow depends on the accretion flow and the outer edge of the central brightness depression [22]. The shadow images for Kerr spacetime with Keplerian accretion disk have been discussed in detail in Refs. [23, 24]. Based on the general relativistic ray-tracing code, the authors in [25] investigated the shadow images of a geometrically thick and infinite thin accretion disk around the compact objects. Recently, wang et al. [26] analyzed shadows of Schwarzschild BH surrounded by a Bach-Weyl ring with the help of the backward ray-tracing procedure. The Bach-Weyl ring is a concentric thin ring that looks like a Newtonian ring of constant density, as introduced in [27]. Inspired by these groundbreaking studies, many other theoretical constraints on BH shadows and some related geometrical properties are discussed in the community, including the shadows with different accretion flow matters and Einstein rings [28–37] etc., based on theoretically well-motivated models. Moreover, the BH shadow has also been analyzed with some interesting physical properties in [38–42]. These heuristics configurations provide us with a realistic description of the shadow dynamics simulations as well as the influences of accretion disk on the BH images.

The theory of GR is regarded as a successful theory only for explaining the gravitational interaction between sub-millimeter and solar system scales [43]. However, Planck's length is generally expected to be replaced by the quantum theory of gravity with ultraviolet completion [44]. Owing to the absence of fundamental quantum gravity, extended theories of gravity, as a phenomenological model representing a classical extension of the GR, were constructed by complying with the recent observational data and the data from local tests. Therefore, it is more interesting to analyze the accreting matter around the BHs in modified gravities. Hence, this study aims to deal with this gap in literature. In the fabric of modified theories, the charged BHs governed by nonlinear electrodynamics (NED) have recently obtained more significance with the development of astrophysical observations. This is the reason for the fact that astrophysical BHs are often carrying strong magnetic fields or immersed in a plasma medium. Therefore, it is interesting to investigate the intrinsic properties of BHs described by NED [45]. In Maxwell's electrodynamics, there exists a singularity at the position of the point charge and has infinite self energy. To deal with this issue, Born and Infeld constructed a nonlinear electromagnetic field [46]. Inspired by this pioneering study, the combination of GR and Born-Infeld field has been investigated to overcome the singularity problem of the BHs as well as some other properties see Refs. [47–49]. Moreover, in the action of effective field theory coming from superstrings, an extended Born-Infeld action occurs naturally as the leading part [50–52].

From the astrophysical point of view, the influence of NED become quite important in super-strongly magnetized compact objects like pulsars and magnetars [53, 54]. More importantly, the first regular BH solution was also investigated as a spherically symmetric solution to GR source by NED, known as Bardeen spacetime [55]. Numerous publications devoted to investigate the intense properties of NED- sourced BHs (see for example Refs. [56–58]). In this regard, Ghosh and Kumar [59] recently proposed a magnetically charged rotating BH model (known as GK BH), coupling the NED to gravity. This BH has a similar type of singularities as illustrated by Kerr BH [60]. The shadow dynamics cast by this BH has been discussed in [61]. In addition, this BH spacetime is closer to Kerr-Newman BH [62] as compared to newly proposed NED triggered rotating regular BHs [63, 64]. More recently, the author in [65] considered the GK rotating BH and studied the scattering states of a massive scalar field and the superradiant amplification process. With the above motivations, this paper aims to investigate the optical features of GK rotating BH spacetime with a spherical background light source along with a thin accretion disk.

The paper will be completed in the following manner. In the upcoming section, we briefly define the review of GK rotating BH coupled with NED and then we investigate the effect of spacetime parameters on the BH shadow images constructed in celestial spheres. In the same section, we will discuss the simulated images of BH shadow within the spherical background light source, which are constructed by imposing the backward ray-tracing method.

By considering geometrically and optically thin accretion disk, in section **III**, we will discuss the observed luminosity of the BH shadow images for values of the associated parameters. Furthermore, a comprehensive investigation will be conducted on the redshift factors for both direct and lensed images of the accretion disk in section **IV**. The last section is devoted to conclusions and discussions.

II. CHARGED ROTATING GHOSH-KUMAR BLACK HOLE AND NULL GEODESICS

The action of GR coupled with NED field is defined as [66]

$$S = \int \sqrt{-g} d^4x \left(\frac{1}{16\pi} \mathcal{R} - \frac{1}{4\pi} \mathcal{L}(F) \right), \quad (1)$$

where \mathcal{R} and g represent the Ricci scalar and the determinant of the metric tensor, respectively. Further, the term $\mathcal{L}(F)$ represents the lagrangian density of the NED having function of the form $F = \frac{1}{4} F^{\mu\nu} F_{\mu\nu}$ with $F_{\mu\nu} = \partial_\mu A_\nu - \partial_\nu A_\mu$, where A_μ is the four-potential. The explicit form of this Lagrangian density can be defined as [59]

$$\mathcal{L} = \frac{4M\sqrt{q}F^{\frac{5}{4}}}{q\left(\sqrt{2} + 2q\sqrt{F}\right)^{\frac{3}{2}}}, \quad (2)$$

in which M and q are BH's mass and magnetic charge, respectively. Applying Newman-Janis algorithm [67] or its extended form [68], one can derive the rotating magnetically charged GK BH in Boyer-Lindquist coordinate, which can be expressed as [59, 65]

$$ds^2 = -\left(1 - \frac{2Mr^2}{\Sigma(r^2 + q^2)^{1/2}}\right) dt^2 + \frac{\Sigma}{\Delta} dr^2 + \Sigma(r, \theta) d\theta^2 - \frac{4aMr^2 \sin^2 \theta}{\Sigma(r^2 + q^2)^{1/2}} dt d\phi + \frac{A(r, \theta)}{\Sigma} \sin^2 \theta d\phi^2, \quad (3)$$

where

$$\begin{aligned} \Sigma &= r^2 + a^2 \cos^2 \theta, \\ \Delta &= r^2 + a^2 - \frac{2Mr^2}{(r^2 + q^2)^{1/2}}, \\ A(r, \theta) &= (r^2 + a^2)^2 - \Delta a^2 \sin^2 \theta, \end{aligned}$$

in which a is the spin parameter. The above metric recovers the Kerr BH solution when $q \rightarrow 0$ and the schwarzschild BH solution when $a = q = 0$ [59]. To study the dynamics of shadows and their associated consequences for rotating BH in strong field approximation, we need to derive geodesic equations by considering Hamilton-Jacobi formulation [69]. The Hamilton-Jacobi equation is given by

$$\frac{\partial S}{\partial \tau} + H = 0, \quad H = \frac{1}{2} g_{\mu\nu} p^\mu p^\nu = -\frac{1}{2} m^2, \quad (4)$$

where τ is the affine parameter, S is the Jacobi action, H is the Hamiltonian, and p^μ is the four-momentum of the particle and m denotes mass of the particle moving in the BH space-time. The component p^μ is defined as

$$p_\mu = \frac{\partial S}{\partial x^\mu} = g_{\mu\nu} \frac{dx^\nu}{d\tau}. \quad (5)$$

Since the Hamiltonian H is independent of t and ϕ , so there are two Killing vectors fields such as, ∂_t and ∂_ϕ as translational and rotational invariance of time, produce two constants of motion: conserved energy $E = -p_t$ and conserved angular momentum $L = p_\phi$ about the axis of symmetry [70]. The components p_t and p_ϕ are generalized momenta in respective directions. The Jacobi action S of the photon can be separated into the following form

$$S = \frac{1}{2} m^2 \tau - Et + L\phi + D_r(r) + D_\theta(\theta), \quad (6)$$

where the functions $D_r(r)$ and $D_\theta(\theta)$ depend only on r and θ , respectively yet to be determined. For photon, $m = 0$. Putting Eq. (6) in Hamilton-Jacobi equation and then by introducing the Carter constant \mathcal{Q} [71], one obtains

$$D_r(r) = \int^r \frac{\sqrt{R(r)}}{\Delta} dr, \quad D_\theta(\theta) = \int^\theta \sqrt{\Theta(\theta)} d\theta, \quad (7)$$

with

$$\begin{aligned} R(r) &= (E(r^2 + a^2) - aL)^2 - \Delta(\mathcal{Q} + (L - aE)^2), \\ \Theta(\theta) &= \mathcal{Q} + \left(a^2 E^2 - \frac{L^2}{\sin^2 \theta} \right) \cos^2 \theta, \end{aligned} \quad (8)$$

where Δ is defined in Eq. (3). Then, the variations of the Jacobi action give rise to the following geodesic equations, given as

$$\begin{aligned} \Sigma \frac{dt}{d\tau} &= a(L - aE \sin^2 \theta) + \frac{r^2 + a^2}{\Delta} (E(r^2 + a^2) - aL), \\ \Sigma \frac{dr}{d\tau} &= \pm \sqrt{R(r)}, \\ \Sigma \frac{d\theta}{d\tau} &= \pm \sqrt{\Theta(\theta)}, \\ \Sigma \frac{d\phi}{d\tau} &= \frac{L^2}{\sin^2 \theta} - aE + \frac{a}{\Delta} (E(r^2 + a^2) - aL). \end{aligned} \quad (9)$$

The sign \pm corresponds to the positive and negative momentum, Respectively, i.e., the direction of moving particle. Since we are interested in analyzing the boundary of the shadow cast by the rotating GK BH, so we consider the geodesic equation which can be written as

$$\frac{1}{2} \left(\Sigma \frac{dr}{d\tau} \right)^2 + V(r) = 0, \quad (10)$$

where $V(r)$ is the effective potential that can be defined as $V(r) = -R(r)/2r^4$ and in the equatorial plane ($\theta = \pi/2$). The maximum value of the $V(r)$ corresponds to the position of the unstable photon orbit. The BH shadow silhouette is derived from the specific orbit in the radial equation, defined by $r = r_{ph}$, which satisfies the underlying conditions [73]

$$V(r)|_{r=r_{ph}} = 0, \quad \frac{\partial V(r)}{\partial r} \Big|_{r=r_{ph}} = 0. \quad (11)$$

The motion of a photon is determined by two impact parameters

$$\xi = \frac{L}{E}, \quad \eta = \frac{\mathcal{Q}}{E^2}, \quad (12)$$

which parameterize the null geodesics. Solving Eq. (11), one can obtain the following expressions of the critical values of impact parameters (ξ_{cr} , η_{cr}) for the unstable photon orbits as

$$\xi_{cr} = \frac{(a^2 + r_{ph}^2)\Delta'(r_{ph}) - 4r_{ph}\Delta(r_{ph})}{a\Delta'(r_{ph})}, \quad (13)$$

$$\begin{aligned} \eta_{cr} &= (r_{ph}^2(-16\Delta(r_{ph})^2 - r_{ph}^2\Delta'(r_{ph})^2 + 8\Delta(r_{ph})(2a^2 \\ &+ r_{ph}\Delta'(r_{ph}))))(a^2\Delta'(r_{ph})^2)^{-1}, \end{aligned} \quad (14)$$

here ($'$) denotes the derivative with respect to r . Now, we are going to analyze the significant features of the free-moving matter around BH spacetime geometry. In general, the photons emitted by a light source are deflected when they pass near a BH due to strong gravitational lensing. Some of them, after being deflected by the BH, can reach a distant observer, while others fall directly into the BH. The photons that cannot escape from the BH shadow are in the observer's sky. So, we introduce the celestial coordinates, connected to the actual astronomical measurements that span a two dimensional plane, written as [74, 75]

$$X = \lim_{r_{obs} \rightarrow \infty} \left(-r_{obs}^2 \sin \theta_{obs} \left(\frac{d\phi}{dr} \right)_{(r_{obs}, \theta_{obs})} \right), \quad (15)$$

$$Y = \lim_{r_{obs} \rightarrow \infty} \left(r_{obs}^2 \left(\frac{d\theta}{dr} \right)_{(r_{obs}, \theta_{obs})} \right), \quad (16)$$

here r_{obs} is the radial coordinate position of the observer, lie far away from the BH, and θ_{obs} is the inclination angle of the observer. Now Eqs. (15) and (16) can be further simplified in terms of impact parameters as [75]

$$X = -\xi_{cr} \csc \theta_{obs}, \quad (17)$$

$$Y = \pm \sqrt{\eta_{cr} + a^2 \cos^2 \theta_{obs} - \xi_{cr}^2 \cot^2 \theta_{obs}}. \quad (18)$$

If the observer is located on the equatorial plane, i.e., $\theta_{obs} \rightarrow \pi/2$, the above equations can be simplified as

$$X = -\xi_{cr}, \quad (19)$$

$$Y = \pm \sqrt{\eta_{cr}}. \quad (20)$$

To analyze the shape and size of the shadow for an equatorial observer in the strong field region, we plot the shadow images of rotating GK BH for various values of a and q in Fig. 1. The left panel shows the circular orbit for different values of spin parameter a . It is observed that with the aid of a , the circular orbits are shifted in the positive x -direction. For smaller values of a , the shadow images can be identified as perfect circles. However, when $a = 1$, the shadow images move rightwards with an elongation in the shadow and exhibit a clear possible flatness on the left side of the shadow, see Fig. 1 (a). In Fig. 1 (b), very small differences are measured in the shadows with the variation of NED parameter q . The image size reduced with increasing q and the shadow images can be identified as perfect circles when q has lesser values. With an increase in the value of q , the shadow images are slightly moved towards the positive x -direction and negligible flatness is being observed on the left side of the shadow images when $q \rightarrow 1$. This deforms the perfect circles into oval geometry. These effects and differences of images will be discussed in the upcoming sections, which may serve as a criterion to distinguish GK rotating BHs from other spacetimes.

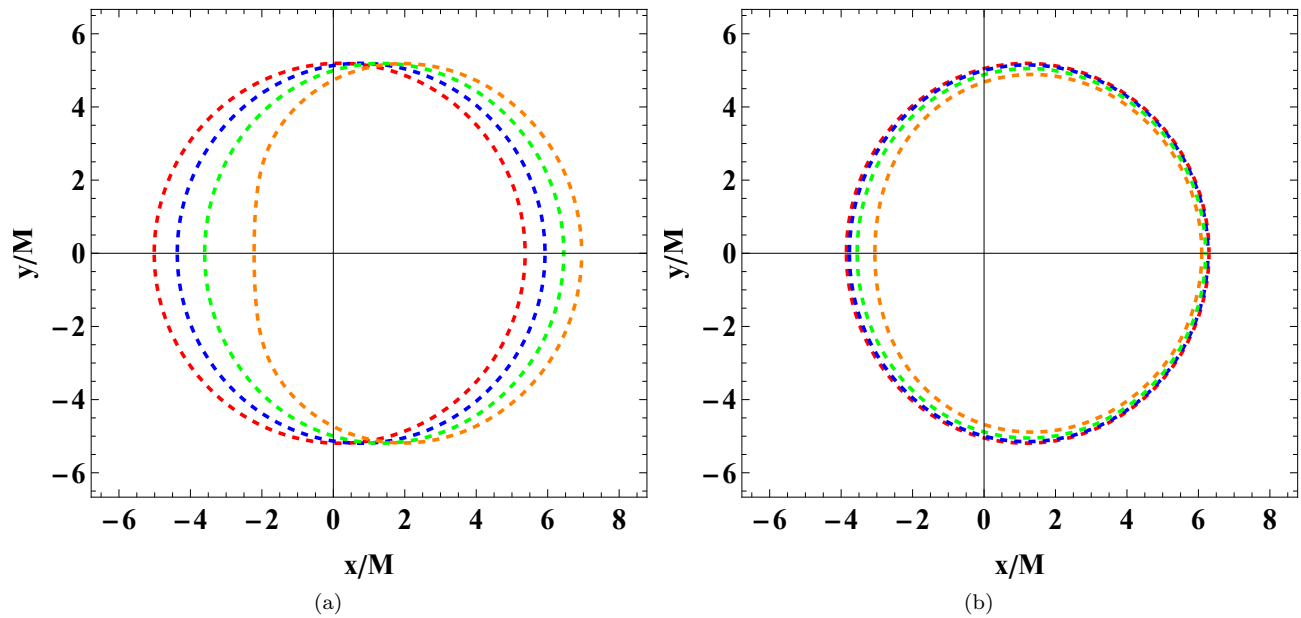


FIG. 1: Figure (a) illustrates the circular orbits for different values of $a = 0.1, 0.4, 0.7, 1$, corresponding to red, blue, green and orange dashed curves, respectively for fixed $q = 0.1$. Whereas Fig. (b) illustrates the circular orbits for different values of $q = 0.1, 0.4, 0.7, 1$, corresponding to red, blue, green and orange dashed curves, respectively with fixed $a = 0.6$. Both cases are observed for fixed $M = 1$ and $\theta_{obs} = 80^\circ$.

A. Shadow Images Under Spherical Background Light Source

Now we discuss the optical appearance of BH shadow images with the help of a well-known numerical backward ray-tracing method which has been widely used in literature [26, 76–85]. In the present study, we will provide the essential steps of this method, which may be fruitful for the readers. In this setup, one can assume that the light rays evolve from the observer reverse in time. After that, one can define the position of each pixel in the final image by

solving the null geodesic equations numerically. Here, the optical appearance of BH shadow in the observer's screen is suppressed by the pixels connected to the photons that directly fall into the BH. We assume that an observer is located at (r_{obs}, θ_{obs}) in the coordinated (t, r, θ, ϕ) . In this scenario, one can expand the observer basis $(e_{\hat{t}}, e_{\hat{r}}, e_{\hat{\theta}}, e_{\hat{\phi}})$ as a form on the coordinate basis [26, 76–85]

$$e_{\hat{\mu}} \equiv e_{\mu}^{\nu} \partial_{\nu}, \quad (21)$$

in which the matrix e_{μ}^{ν} satisfies $g_{\mu\nu} e_{\xi}^{\mu} e_{\zeta}^{\nu} = \varpi_{\xi\zeta}$, where $\varpi_{\xi\zeta}$ is the Minkowski spacetime. For spacetime (3), it is convenient to choose a decomposition

$$e_{\hat{\mu}}^{\nu} = \begin{pmatrix} \sigma & 0 & 0 & \rho \\ 0 & \mathcal{A}^r & 0 & 0 \\ 0 & 0 & \mathcal{A}^{\theta} & 0 \\ 0 & 0 & 0 & \mathcal{A}^{\phi} \end{pmatrix}, \quad (22)$$

here $\sigma, \rho, \mathcal{A}^r, \mathcal{A}^{\theta}$, and \mathcal{A}^{ϕ} are real coefficients. Further, Eq. (22) is related to zero angular momentum observer in relation to spatial infinity. Based on the Minkowski normalization $e_{\hat{\mu}} e^{\hat{\nu}} = \delta_{\hat{\mu}}^{\hat{\nu}}$, one can obtain the following relations

$$\begin{aligned} \mathcal{A}^r &= \frac{1}{\sqrt{g_{rr}}}, & \mathcal{A}^{\theta} &= \frac{1}{\sqrt{g_{\theta\theta}}}, & \mathcal{A}^{\phi} &= \frac{1}{\sqrt{g_{\phi\phi}}}, \\ \sigma &= \sqrt{\frac{g_{\phi\phi}}{g_{t\phi}^2 - g_{tt}g_{\phi\phi}}}, & \rho &= -\frac{g_{t\phi}}{g_{\phi\phi}} \sqrt{\frac{g_{\phi\phi}}{g_{t\phi}^2 - g_{tt}g_{\phi\phi}}} \end{aligned} \quad (23)$$

From Eq. (21), the locally measured 4-momentum of a photon $p^{\hat{\mu}}$ can be defined as

$$p^{\hat{t}} = -p_{\nu} e_{\hat{t}}^{\nu}, \quad p^{\hat{i}} = p_{\nu} e_{\hat{i}}^{\nu}, \quad (24)$$

where $(\hat{i} = r, \theta, \phi)$. Hence, the locally measured 4-momentum of coupled photons $p^{\hat{\mu}}$ can be redefined as

$$\begin{aligned} p^{\hat{t}} &= \sigma E - \rho L, & p^{\hat{\phi}} &= \frac{L}{\sqrt{g_{\phi\phi}}}, \\ p^{\hat{\theta}} &= \frac{p_{\theta}}{\sqrt{g_{\theta\theta}}}, & p^{\hat{r}} &= \frac{p_r}{\sqrt{g_{rr}}}, \end{aligned} \quad (25)$$

where p_{θ} and p_r are the components of momentum of the photon $p_{\theta} = g_{\theta\theta} \frac{d\theta}{d\tau}$ and $p_r = g_{rr} \frac{dr}{d\tau}$, respectively. The three vector \vec{p} is the linear momentum of photons having components $(p^{\hat{r}}, p^{\hat{\theta}}, p^{\hat{\phi}})$ in the orthonormal basis $(e_{\hat{r}}, e_{\hat{\theta}}, e_{\hat{\phi}})$ as [86]

$$\vec{p} = p^{\hat{r}} e_{\hat{r}} + p^{\hat{\theta}} e_{\hat{\theta}} + p^{\hat{\phi}} e_{\hat{\phi}}. \quad (26)$$

Based on the geometry of the photon's observables, we have [86]

$$\begin{aligned} p^{\hat{r}} &= |\vec{p}| \cos \mathbb{A} \cos \mathbb{B}, \\ p^{\hat{\theta}} &= |\vec{p}| \sin \mathbb{A}, \\ p^{\hat{\phi}} &= |\vec{p}| \cos \mathbb{A} \sin \mathbb{B}, \end{aligned} \quad (27)$$

where (\mathbb{A}, \mathbb{B}) are the angular coordinates of a point in the local observer's sky, interpreting the orientation of the associated photon and develop its initial conditions. Closely followed by similar steps [26, 76–86], one can obtain the celestial coordinates (X, Y) for the pixel corresponding to light ray which is defined as

$$\begin{aligned} X &= -r_{obs} \tan \mathbb{B} = -r_{obs} \frac{p^{\hat{\phi}}}{p^{\hat{r}}}, \\ Y &= r_{obs} \frac{\tan \mathbb{A}}{\cos \mathbb{B}} = r_{obs} \frac{p^{\hat{\theta}}}{p^{\hat{r}}}. \end{aligned}$$

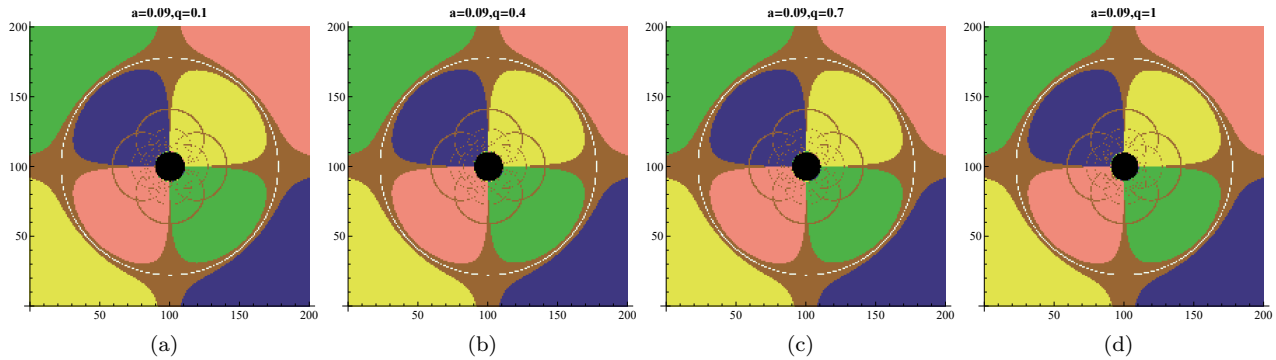


FIG. 2: The shadow images cast by rotating GK BH for different values of q . Here, we fixed $M = 1$, $a = 0.09$, $r_{obs} = 500M$ and the inclination angle of the observer is $\theta_{obs} = 80^\circ$.

In this scenario, for the spacetime (3), one can define the observational position of the image produced due to the photon in observer's sky as

$$\begin{aligned}
 X &= -r_{obs} \frac{p^{\hat{\phi}}}{p^{\hat{r}}} = -r_{obs} \frac{\Delta \sqrt{g_{rr}} L}{\sqrt{g_{\phi\phi} R(r_{obs})}}, \\
 Y &= r_{obs} \frac{p^{\hat{\theta}}}{p^{\hat{r}}} = r_{obs} \frac{\Delta \sqrt{g_{rr}} p^\theta}{\sqrt{g_{\theta\theta} R(r_{obs})}},
 \end{aligned} \tag{28}$$

where $r = r_{obs}$ and $\theta = \theta_{obs}$. Previously, we defined the celestial coordinates in Eqs. (15) and (16), these results are employed only when a real observer lies far away from the BH such as $r_{obs} \rightarrow \infty$. In this way, we have shown the optical appearance of shadow images of the considering BH spacetime in the celestial sphere with the help of backward ray-tracing method in Figs. 2-4 for different values of a and q . Similarly, as done in Refs. [26, 76–85], for the comprehensive physical interpretation of shadow images, one can classify the celestial sphere into four different quadrants mark with colours (♠, ♣, ♠, ♣). The grid of both longitude and latitude lines is denoted by brown lines positioned by 10° . The dark area in the center of each panel shows the BH, where photons directly fall into the BH. In each panel, outside the “D” shape petals, there is a white circular curve which could provide a direct interpretation of Einstein ring. In Fig. 2, we interpret the shadow casted by rotating GK BH for different values of parameters q with fixed $a = 0.09$. Here we see that from left to right as the values of parameter q grow the shadow's shape is a perfect circle, which is similar to those of the usual static BHs. However, with the aid of q , from left to right the size of the shadow decreases negligibly. Importantly, when $q = 1$, the Einstein ring is vertically divided into two equal parts, which shows the effect of NED on the shadow of the BH. Similarly, when we increase the values of spin parameter $a = 0.69$ and parameter $q = 0.1, 0.3, 0.5, 0.7$ varies from left to right in Fig. 3, we notice that the Einstein ring shows the arcs like shapes in the middle of the screen. Moreover, with increasing q , from left to right the shadow shape is a perfect circle and remains the same in all cases. When we further increase the value of $a = 0.99$ and choose the smaller values of q as compared to previous cases such that, $q = 0.01, 0.03, 0.05, 0.07$ corresponds to Fig. 4 (a-d), again the Einstein ring shows the arcs like shapes in the middle of the screen. But these arcs are smaller as compared to the previous one. Again, the size of the shadow is the same and the white light arc is negligibly dispersed with the aid of q . In all cases, we observed a common phenomenon which is the dark area as well as “D” shape petals remain the same. These distinct features in the shadow can be attributed to the effect of the spin and NED parameters i.e., a and q on the spacetime structures. These results may differentiate the rotating GK BH from other spacetime structures.

III. DYNAMICS OF BLACK HOLE SHADOW WITHIN A THIN DISK ACCRETING FLOW

The analysis of accreting disk around BHs provides a crucial entrance for deepening our comprehension of the vital physical mechanisms governing these intricate systems. This section is devoted to advancing our comprehension through an investigation into the observable attributes of accretion disks within the paradigm of considering spacetime. We hope this analysis elucidates the distinctive impact on the observable features of accretion disk structures that arise from modifications to the geometric properties of spacetime within the rotating GK BH paradigm. It is fascinating

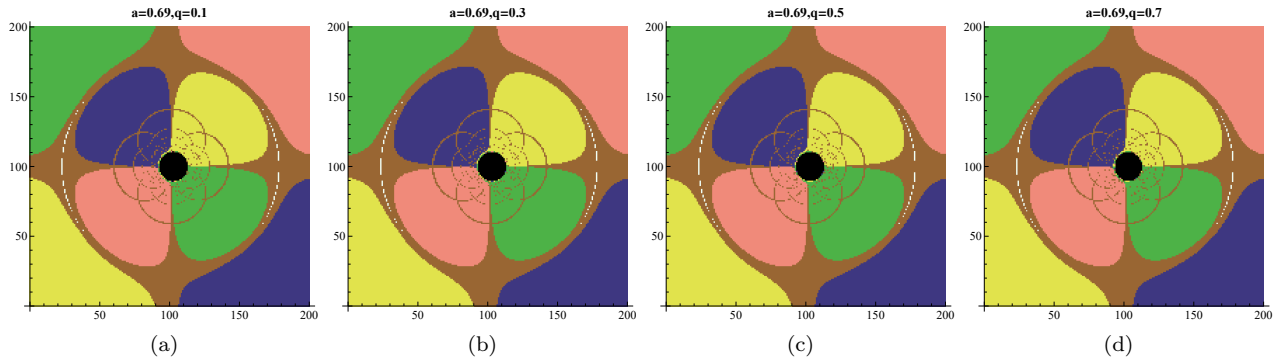


FIG. 3: The shadow images cast by rotating GK BH for different values of q . Here, we fixed $M = 1$, $a = 0.69$, $r_{obs} = 500M$ and the inclination angle of the observer is $\theta_{obs} = 80^\circ$.

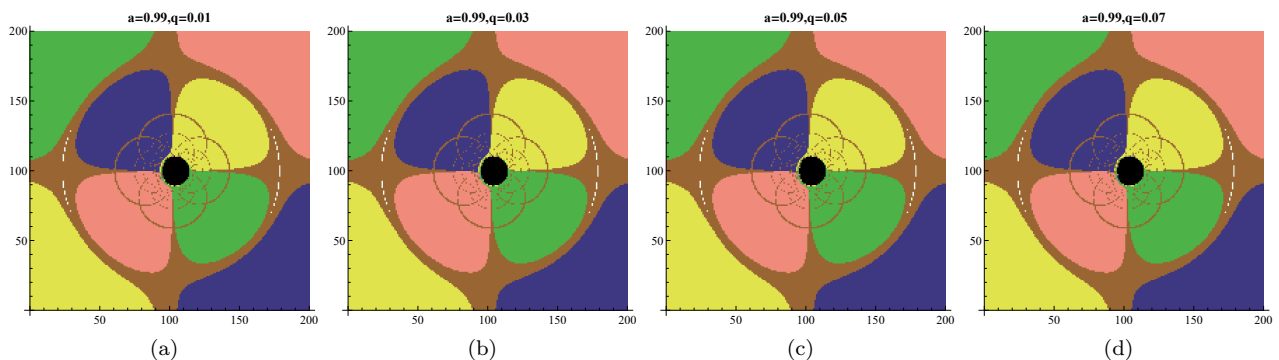


FIG. 4: The shadow images cast by rotating GK BH for different values of q . Here, we fixed $M = 1$, $a = 0.99$, $r_{obs} = 500M$ and the inclination angle of the observer is $\theta_{obs} = 80^\circ$.

to analyze numerous specific aspects that we take into account in this accretion model. Since we assume that the accreting matter is electrically free neutral plasma and moves along an equatorial timelike geodesic. Moreover, in the examination of the BH accretion disk, the radii of the BH provide significant factors about the shadow of the BH. The inner stable circular orbit (ISCO) are related to the inner boundary of the accretion disk around the BH and their radii can be used to compute the energy emission efficiency, which is a measure of how quickly energy from the rest mass turns into radiation. The mechanism of these particles during this process has been analyzed with astrophysical observations [87]. The ISCO indicates a demarcation line, outside this the emission spectrum of the accretion disk will maintain stable circular orbits, while inside the boundary they will undergo critical plunging orbits. Now, we would like to define the circular orbits of the particles that lie within the range $r \geq r_{ISCO}$, which should satisfy the condition, defined in Eq. (11). However, for the range $r < r_{ISCO}$, one can define the radial motion U_r as given below

$$U_r = -\sqrt{-\frac{V(r)}{g_{rr}}}, \quad (29)$$

where the (“-”) sign in front of the square root means the inward motion of particles. Notably, in our examination when tracing the associated light ray backwards, it may cross the equatorial plane many times, having different radii of intersections. Letting $r_n(X, Y)$ represents the radius at which a ray intersects the equatorial plane for the n^{th} time on its backward journey from screen position (X, Y) . Moreover, the function $r_n(X, Y)$ is so-called the radiative transport, which is governed by the Boltzmann equation for photons. This function generates the shape of the n^{th} image of the disk. For example, when $n = 1$, it corresponds to *direct* image and $n = 2$ corresponds to *lensed* image, which is produced on the screen. Importantly, the radiative transfer function closely depends on the observational angle θ_{obs} and algorithms used here typically form images, where each pixel on the image corresponds to a wave vector.

In this scenario, we still consider the screen in the frame of zero angular momentum and the intensity of the

accretion disk naturally change due to the emission and absorption of light rays when they reaches the accretion disk. For the sake of convenience, we assume that the scattering is negligible and the equation which is used to determined the change of intensity can be defined as the following familiar form [88–92]

$$\frac{d\mathcal{I}}{d\tau} = \mathcal{J} - \mathcal{C}\mathcal{I}, \quad (30)$$

where $\mathcal{I} = I_\nu/\nu^3$, $\mathcal{J} = J_\nu/\nu^2$ and $\mathcal{C} = \alpha_\nu\nu$. Further, the components I_ν (cgs units: $\text{erg cm}^{-2} \text{s}^{-1} \text{sr}^{-1} \text{Hz}^{-1}$), J_ν , (cgs units: $\text{erg cm}^{-3} \text{s}^{-1} \text{sr}^{-1} \text{Hz}^{-1}$), α_ν (cgs units: erg cm^{-1}) denotes specific intensity, emissivity per unit volume and absorption coefficient with frequency ν , respectively. Notice that, when the beams of light propagating in different directions at a single point in space, both J_ν , and α_ν approaches to zero and hence the quantities I_ν/ν^3 is conserved along the geodesic.

Moreover, we assume that spinning spacetime is stationary, axisymmetric, and reflection-symmetric about the equatorial plane. Since the accretion disk is geometrically thin, the coefficient of emissivity and absorption remains constant when the light rays cross it. Integrating Eq. (30), one can obtain the final form of intensity on the observer's screen, given as below (the readers can see the complete derivation in Ref. [90])

$$I_{\nu_{obs}} = \sum_{n=1}^m \left(\frac{\nu_{obs}}{\nu_n} \right)^3 \frac{J_n}{\Phi_n - 1} \left(\frac{1 - e^{-\alpha_n \mathcal{F}_n}}{\mathcal{F}_n} \right), \quad (31)$$

where ν_{obs} indicates the observed frequency by the observer, ν_n represents the frequency observed by the local static frames co-moving with the emission profiles and m is the maximum number of intersections on the screen position (X, Y) . Further, we consider the class of frames $\{\mathbb{F}_n\}$, where $n = 1 \dots m(X, Y)$ is the maximum number of times that the light ray passes the equatorial plane, and the subscript n represents the corresponding measurements in the static local frames \mathbb{F}_n . The component Φ_n is the optical depth of photons change accordingly when they are emitted at N defined as

$$\Phi_N = \begin{cases} \exp(\sum_{n=1}^N \alpha_n \mathcal{F}_n) & \text{if } N \geq 1, \\ 1 & \text{if } N = 0, \end{cases} \quad (32)$$

with $\mathcal{F}_n = \nu_n \Delta\tau_n$ a fudge factor to account for the effects of geometrical thickness, further related with to artificially enhances the flux in the photon rings. Moreover, it is a highly defensible fudge, allowing the equatorial approximation, leading to the enhancement of its simplicity and speed [20]. In the fudge factor, the quantity of the component $\Delta\tau_n$ is the change in the affine parameter when the particular ray passing through the accretion disk medium at \mathbb{F}_n . When we consider the optically thin accretion disk means that we safely ignore the absorption effect, then Eq. (31) reduce to the following form

$$I_{\nu_{obs}} = \sum_{n=1}^m \mathcal{F}_n \mathbf{g}_n^3(r_n, X, Y) J_n, \quad (33)$$

where \mathbf{g}_n is the redshift factor, which is $\mathbf{g}_n = \nu_{obs}/\nu_n$. Since, the emission spectrum of particles can be categorized into two different regions based on the ISCO, the redshift factor of the accretion disk within and beyond the ISCO display perceptible differences. Firstly, particles lying beyond the ISCO move along a circular orbit having angular velocity Γ , associated with the redshift factor can be defined as

$$\mathbf{g}_{cir} = \frac{\hat{E}}{(1 - \Gamma_n \mathbf{b})\chi}, \quad r_n \geq r_{ISCO}, \quad (34)$$

where

$$\Gamma_n(r) = \frac{U^\phi}{U^t} \Big|_{r=r_n}. \quad (35)$$

In Eq. (34) the term \mathbf{b} is the impact parameter, defining the ratio of energy and angular momentum of photon along null geodesics, χ is angular velocity function and \hat{E} is the ratio of observed energy on the image plane to the conserved energy along null geodesics. Mathematically, these components can be defined as

$$\mathbf{b} = \frac{L_n}{E_n}, \quad \hat{E} = \frac{E_n}{E_n^o} = \sigma + \hat{E}\rho, \quad \chi = \sqrt{\frac{-1}{g_{tt} + 2g_{t\phi}\Gamma_n + g_{\phi\phi}\Gamma_n^2}} \Big|_{r=r_n}, \quad (36)$$

where E_n^o is the observed energy of the photon. Importantly, when $r_{obs} \rightarrow \infty$, then $\widehat{E} \rightarrow 0$ for the asymptotically flat spacetimes. Now, the particles are moving along the critical plunge orbit, lie inside the ISCO, and then the redshift factor has the following form

$$\mathbf{g}_{plu} = -\frac{\widehat{E}}{U_r p_r / E_n + E_i (g^{tt} - \mathbf{b}g^{t\phi}) + L_i (\mathbf{b}g^{\phi\phi} - g^{t\phi})} \Big|_{r=r_n}, \quad r_n < r_{ISCO}, \quad (37)$$

where E_i and L_i are the energy and the angular momentum of the photon on ISCO, respectively. A similar treatment was used to analyze the images of Kerr BHs in Refs. [20, 93]. Moreover in [87, 90, 94], authors employed Eq. (33) and analyzed different dynamics of simulated images of Kerr geometry surrounded by an optically thin accretion disk, having central brightness depression and a narrow bright photon ring. Specifically, considering the ratio of the observation wavelength (1.3 mm), which is consistent with the images of M87 and Sgr A* at 230 GHz, we define the emissivity to be a second-order polynomial in log-space as

$$\log[J] = (\rho_1 k^2 + \rho_2 k), \quad (38)$$

with $k = \log(\frac{r}{r_+})$. To interpret 230 GHz images in this paper, we set $\rho_1 = -1/2$ and $\rho_2 = -2$ for better visual appearance [87, 90]. In addition, the roots of Δ correspond to the horizons of the BH, and we choose here the largest root (r_+) for the value of the event horizon of the BH. Since the emission profile is isotropic and axisymmetric and decaying rapidly with respect to the horizon r_+ . In [87], authors worked with different choices of \mathbb{F}_n , we normalize all the fudge factors \mathbb{F}_n to 1 [90]. Because we mainly focused on discussing the influence of magnetic fields on the emission profiles, as the values of \mathbb{F}_n vary the optical appearance of the photon ring negligibly, which has very limited influence on overall image. In this scenario, we use Eq. (33) and plot the corresponding emission profiles for different choices of the model parameters.

A. Optical Signatures of the Black Hole Shadow Images

In this subsection, we will briefly define the physical interpretation of the prograde accretion disks surrounding the GK rotating BH within our theoretical framework. In Fig. 5, we illustrate the density profiles illuminated by prograde flows for different values of q and the observational angle θ_{obs} with fixed values of $a = 0.69$ and $M = 1$. Initially, in the left and middle columns of Fig. 5 where $\theta_{obs} = 0.01^\circ$ and 17° , respectively, the observational representation of bright band around the BH shows that the intensity distribution is so sharp that the direct and lensed images are hard to distinguish. However, with increasing observational angle $\theta_{obs} = 80^\circ$, as shown in the right column of Fig. 5, from top to the bottom one can see that the luminosity of the accretion disk is dim as compared to the previous one. Moreover, a gradual metamorphosis transpires appeared, wherein the disk-like structure gradually transforms into a configuration reminiscent of a hat. And here, at the event horizon $r = r_+$, the boundary of the hat-like shape of the BH shows direct images of the accretion disk and the region outside the white dashed ring (which is hard to see) shows the lensed images of the accretion disk. In addition, the radiation flux intensity illustrates a progressively growing asymmetry between the left and right facets of the accretion disk. This emphasized asymmetry is rooted in the heightened influence of the Doppler effect with the addition of the observation angle. Consequently, the disparity in radiant flux intensity between the left and right sides of the accretion disk magnifies significantly with the aid of the observation angle.

The origin of this phenomenon can be observed in the relative motion between the observer and the accretion flows emitted within the confines of the accretion disk. Note that, the inner shadow is from the fact that a light ray cannot obtain any intensity if directly falling into the horizon without passing the equatorial plane such as $m = 0$. In Fig. 6, we further present the density profiles for three different values of NED parameter q with fixed inclination angle $\theta_{obs} = 80^\circ$, $a = 0.69$ and $M = 1$. Here we observe that initially, when q has smaller values such as $q = 0.001$, the white dashed circle only shows at the bottom of the hat-like shape and on the left side of the screen, we see significant Doppler effects due to the forward rotation of the prograde accretion disk. All these effects can be seen more clearly when $q = 0.01$ and 0.99 . This leads to changes in the NED parameter q , each image exhibits a distinct photon ring as well as Doppler effects on the left side of the screen.

Table 1. The maximal blueshift under different spin and NED parameters a and q , respectively. All data are sourced from direct images, with $M = 1$, an observational angle of $\theta_{obs} = 80^\circ$, and prograde motion.

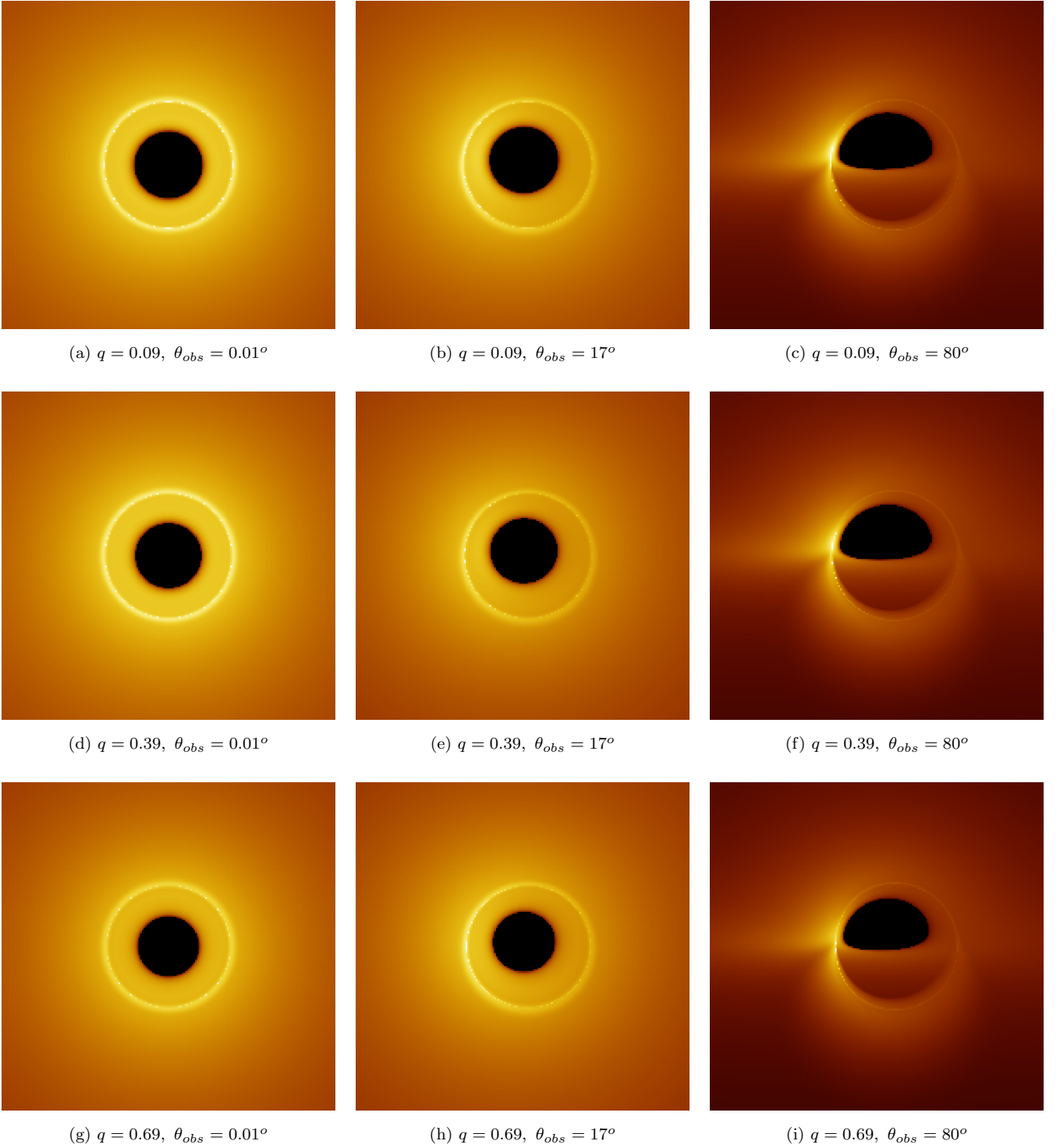


FIG. 5: Density profiles of GK rotating BH illuminated by prograde flows. Columns from left to right display models with inclination angle $\theta_{obs} = 0.01^\circ, 17^\circ, 80^\circ$ and rows from top to bottom display with NED parameters $q = 0.09, 0.39, 0.69$. The filled black area is the BH event horizon. For all images, we set $a = 0.69, M = 1$ and the observer's position is fixed at $r_{obs} = 500M$.

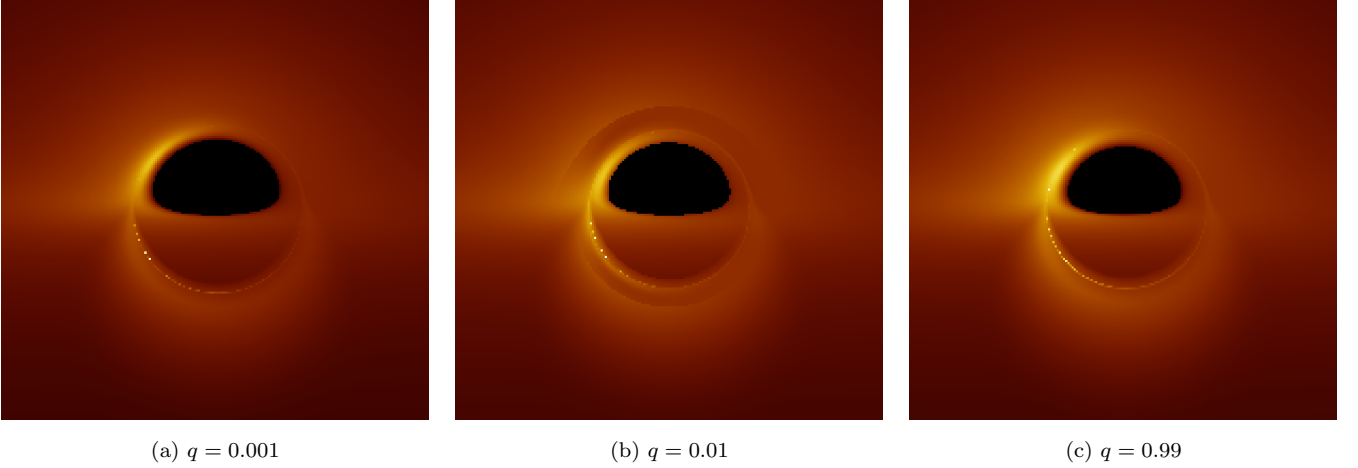


FIG. 6: Density profiles of GK rotating BH is illuminated by prograde flows. The filled black area is the BH’s event horizon. The white dashed circle close to the lensed horizon known as “photon ring”. For all images, we fixed inclination angle $\theta_{obs} = 80^\circ$, $a = 0.69$, $M = 1$ and the observer’s position is fixed at $r_{obs} = 500M$.

		\mathbf{g}_{\max}					
a \ q	0.09	0.19	0.29	0.39	0.49	0.59	0.69
0.09	2.9021	2.4505	2.1595	1.9417	1.7992	1.6943	1.6065
0.19	2.8948	2.4341	2.1437	1.9274	1.7882	1.6838	1.5967
0.29	2.8379	2.4033	2.1152	1.9139	1.7686	1.6749	1.5791
0.39	2.7731	2.3554	2.0723	1.8909	1.7425	1.6578	1.5616
0.49	2.6823	2.2881	2.0220	1.8560	1.7168	1.6298	1.5436
0.59	2.5654	2.2008	1.9835	1.8072	1.6836	1.5941	1.5084
0.69	2.4450	2.1433	1.9252	1.7696	1.6483	1.5580	1.4607

Table 2. The maximal blueshift under different spin and NED parameters a and q , respectively. All data are sourced from lensed images, with $M = 1$, an observational angle of $\theta_{obs} = 80^\circ$, and prograde motion.

		\mathbf{g}_{\max}					
a \ q	0.09	0.19	0.29	0.39	0.49	0.59	0.69
0.09	1.1873	1.1955	1.2028	1.2161	1.2345	1.2529	1.2694
0.19	1.1712	1.1899	1.2032	1.2160	1.2327	1.2499	1.2693
0.29	1.1786	1.1886	1.2031	1.2172	1.2328	1.2507	1.2662
0.39	1.1855	1.1889	1.2017	1.2169	1.2327	1.2483	1.2565
0.49	1.1900	1.1942	1.2002	1.2136	1.2283	1.2472	1.3094
0.59	1.1939	1.2037	1.2152	1.2284	1.2533	1.2875	1.3167
0.69	1.1967	1.2098	1.2235	1.2422	1.2681	1.2897	1.3275

IV. EXAMINING THE PROPAGATION OF REDSHIFT FACTORS

Since, the relative motion between the accretion disk and the distant observer, provides a deeper understanding of the intricate interplay among BHs and the resulting properties of accretion disks. These significant results can be understood with the help of the Doppler’s effect. For this, in the imaging process of the BH, we demonstrate an accurate assessment of the redshift factors associated with the behavior of emitting particles.

In Figs. 7 and 8, we present the redshifts factors for different values of model parameters. These include the direct images ($m = 1$) and lensed images ($m = 2$) of the prograde accretion disk. When θ_{obs} has smaller values as shown in top rows of Figs. 7 and 8, no significant influence of the blueshift on the observer’s screen is observed. However, when $\theta_{obs} = 80^\circ$, a significant appearance of the blueshift has been observed on the observer’s screen. This phenomenon

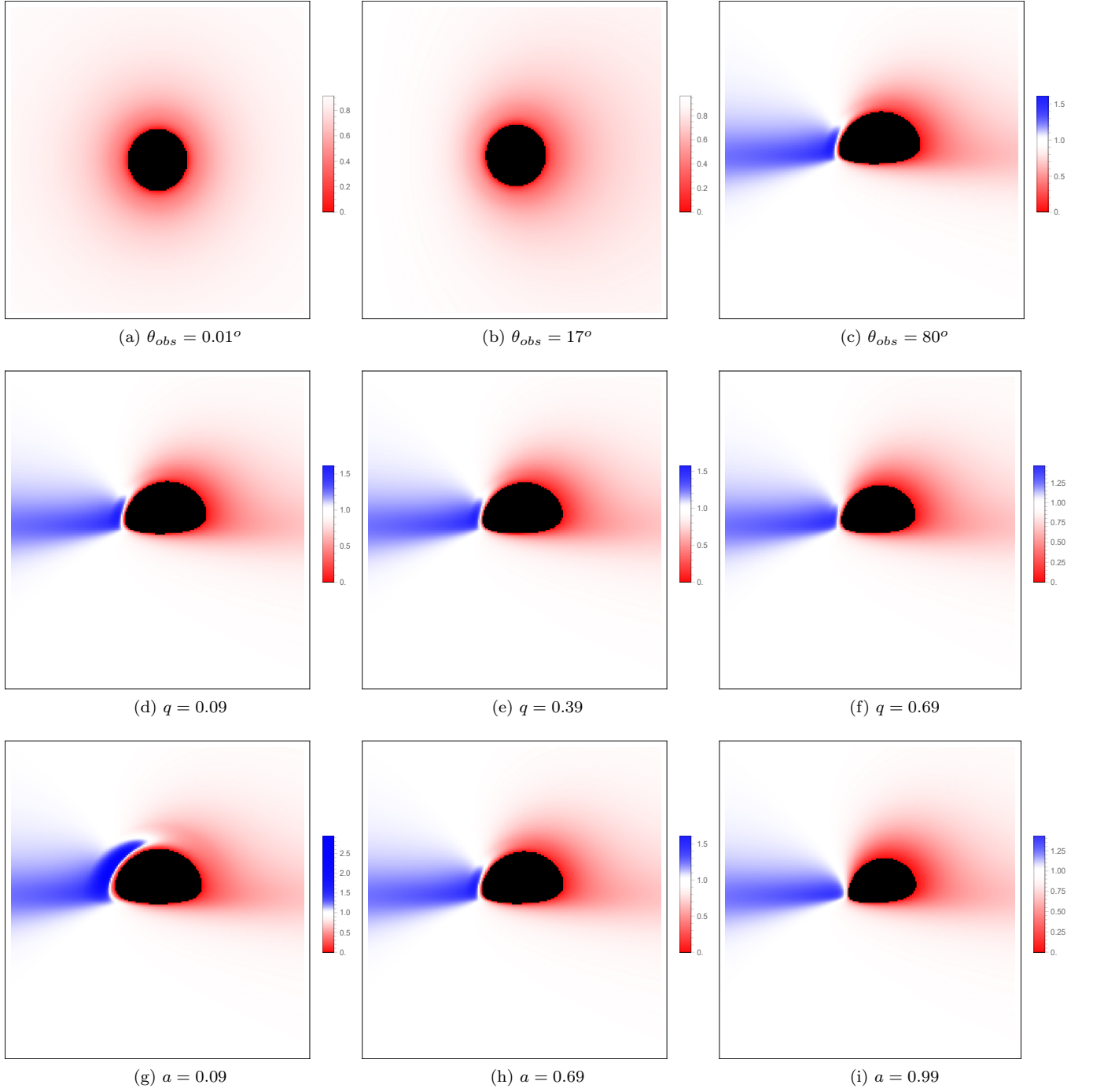


FIG. 7: The direct images of the redshift factors of the considering accretion disk model for different θ_{obs} with fixed $a = 0.69$, $q = 0.09$ (top row), for different q with fixed $a = 0.69$, $\theta_{obs} = 80^\circ$, (middle row) and for different a with fixed $q = 0.09$, $\theta_{obs} = 80^\circ$, (bottom row). The red and blue colors indicate the redshift and blueshift, respectively and the filled black area is the BH's event horizon. All these images portray GK rotating BHs, illuminated by a prograde thin equatorial accretion disk with $M = 1$ and the observer's position is fixed at $r_{obs} = 500M$.

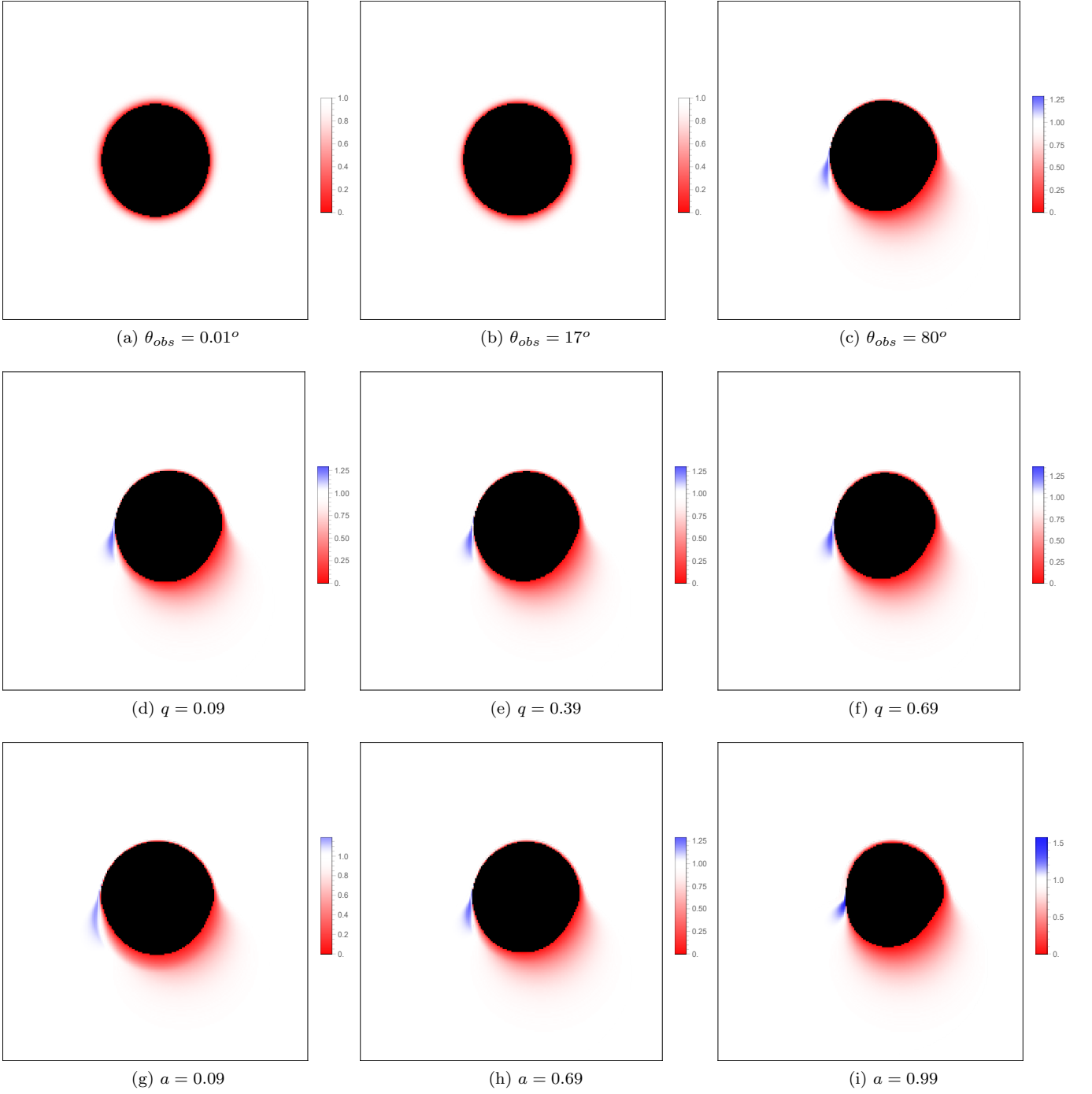


FIG. 8: The lensed images of the redshift factors of the considering accretion disk model for different θ_{obs} with fixed $a = 0.69$, $q = 0.09$ (top row), for different q with fixed $a = 0.69$, $\theta_{obs} = 80^\circ$, (middle row) and for different a with fixed $q = 0.09$, $\theta_{obs} = 80^\circ$, (bottom row). The red and blue colors indicate the redshift and blueshift, respectively and the filled black area is the BH's event horizon. All these images portray GK rotating BHs illuminated by a prograde thin equatorial accretion disk with $M = 1$ and the observer's position is fixed at $r_{obs} = 500M$.

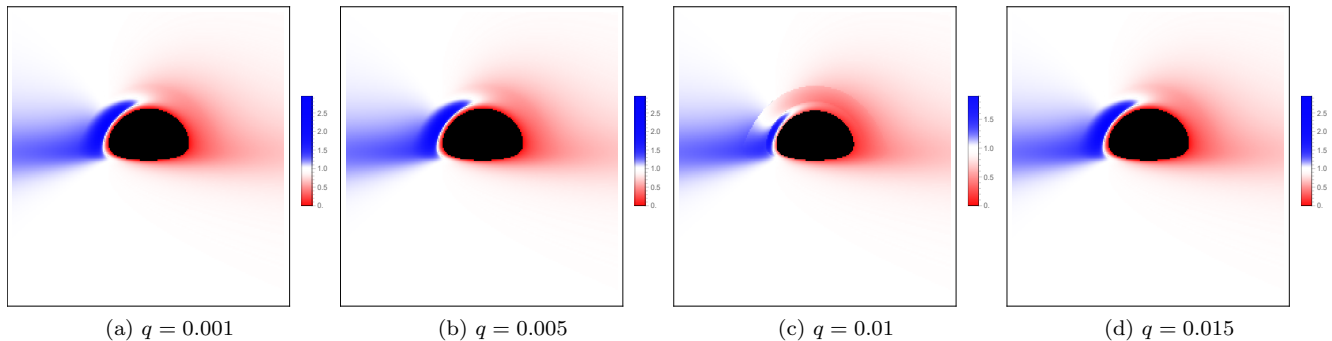


FIG. 9: The direct images of the redshift factors of the considering accretion disk model for different q with inclination angle $\theta_{obs} = 80^\circ$. The red and blue colors indicate the redshift and blueshift, respectively and the filled black area is the BH's event horizon. All these images portray GK rotating BHs illuminated by a prograde thin equatorial accretion disk with $a = 0.09$, $M = 1$ and the observer's position is fixed at $r_{obs} = 500M$.

will happen due to the observer location, the dynamics of the accretion disk rotation, and the significant effect of gravitational redshift from the BHs strong gravitational field. In the second and third rows of Figs. 7 and 8, we present the accretion phenomena with fixed position of the observer such as $\theta_{obs} = 80^\circ$ and analyze the nature of other involved parameters. Here, in the case of direct images, the observer sees a clear bright optical appearance of redshift and blueshift factors on the screen. The variation of parameters corresponds to changes in brightness, indicating different temperatures and densities in the disk. In the case of lensed images, due to the formation of some extra rings or arcs around the BH, the observer can see more prominent redshift factor as compared to blueshift on the screen, see the second and the third rows of Fig. 8. In Fig. 9, we present the influence of smaller values of NED parameter q on the direct images of accretion disk. Initially, when q has smaller values, both red and blue shifts are negligible, merge with each other. However, with the aid of q such as, $q = 0.015$ the redshift moves to the left side of the screen and slightly merge with blueshift. In all these cases, the redshift is closely lie to ISCO. In Tables. 1 and 2, we present the \mathbf{g}_{max} of direct and lensed images, respectively under various values of spin and NED parameters. It is observed from Table. 1 that a and q help to decrease the strength of maximal blueshift factor of direct images on the screen. However, in the case of lensed images, as presented in Table. 2, the maximal strength of blueshift factor on the screen is increased with respect to both spin and NED parameters. All these results are clearly reflects on both direct and lensed images on the screen for prograde accretion disk.

Now, we are going to describe the geometric details of the retrograde accretion disk observed on the observer's screen. As depicted in Fig. 10, the observational representation is suppressed by the gravitational redshift in the scenario of retrograde accretion disk flow. At that frequency, the optical depth suppressing the appearance of the lensed subring, showing on the upper north half of the image on the screen. And the optical depth is more suppressed with the aid of NED parameter q and the optical appearance of the inner shadow is still suppressed. This is due to, during the simulation, the emitting material contributing to the increased total optical depth is contained within the equatorial plane, and the jet material in front of the event horizon shows low brightness. As a result, the direct geometrical effect of the equatorial emission being truncated at the event horizon is still visible, even it is hardly to see [87]. These observations distinctly underscore the profound impact of the NED parameter q on the luminosity and structural stability attributes of the accretion disk that encircles the BH.

In Fig. 11, we presented the redshift factors for direct and lensed images in the top and bottom rows under different values of q . And the accretion flow is retrograded in both cases. In the first row, we notice that the redshift near the ISCO, which will be suppressed by an increase of q . And in the right side of the screen, the influence of redshift lensed curves also appears in the emission of blue shift. This will happen due to the retrograde accretion flow and relativistic jet which lies in front of the bulk of emission in the equatorial plane. In the bottom panel, only on the right side of the screen, a small petal of the blueshift appeared and the redshift factor also lie close to the ISCO. The luminosity of the accretion disk is significantly decreased, because the contribution of the emission flow is smaller due to the lensed images phenomena. consequently, in these simulations, the emission from accretion disk are retrograde emission, which could produce a central brightness depression with a slightly smaller area than the equatorial inner shadow, as the emission region intersects with the event horizon at a maximum latitude on the equatorial plane. We further exhibit the non-uniform resolution used for image computation and storage in Fig. 12. Here the resolution of the bands contains roughly the same number of pixels, resulting in a more manageable number of pixels per image. The complete null geodesic of the GK rotating spacetime is presented with three different bands such as yellow,

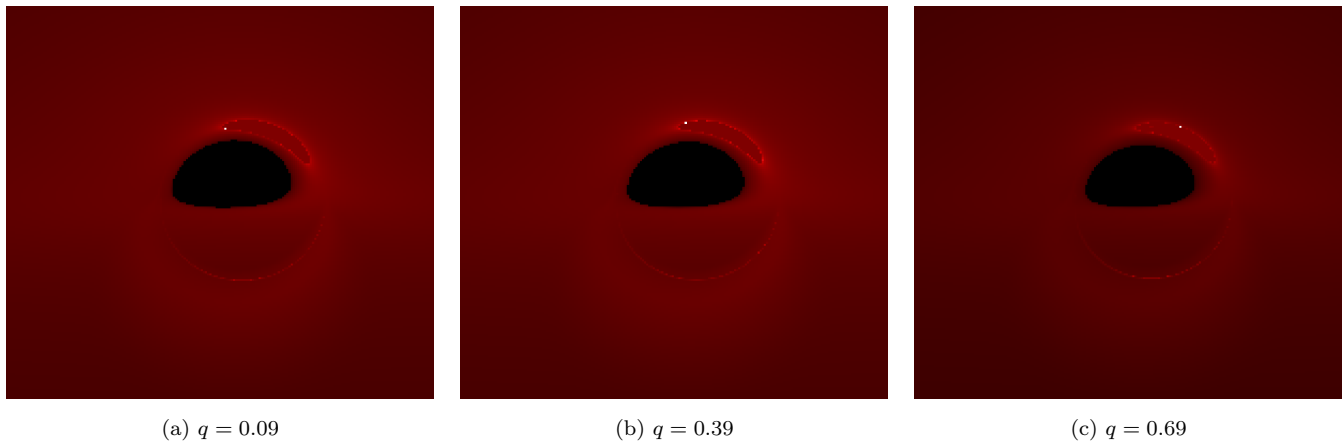


FIG. 10: Density profiles of GK rotating BH are illuminated by retrograde flows. The filled black area is the BH’s event horizon. The white dashed circle close to the lensed horizon known as “photon ring”, which is hard to see here. The slightly prominent white dashed curve is the lensed images of the accretion disk. For all images, we fixed inclination angle $\theta_{obs} = 80^\circ$, $a = 0.69$, $M = 1$ and the observer’s position is fixed at $r_{obs} = 500M$.

blue and green corresponding to the rays that cross the equatorial plane of the BH once, twice, and three times, respectively. In all these cases, the photon rings always lie exactly within the blue and yellow lensing bands. However, the confine shape of blue bands is deformed with change in the observational position and reach the maximum when $\theta_{obs} = 80^\circ$. Hence, the overall discussion about the observation of a BH’s gravitational lensing effect provides an avenue for constraining the involved model parameters on the scale of BHs. We hope these observations may serve as a cornerstone for refining our comprehension of GK rotating BH and its behavior on astronomical scales.

V. CONCLUSIONS AND DISCUSSION

In the last few years, the study of BH spacetime geometry with light rings and accretion disk has become increasingly popular among scientific community, particularly after the beginning of multi-messenger astronomy. The existence of accretion disks surrounding BHs is a well-substantiated phenomenon prompted by a wealth of empirical evidence. An important milestone was reached with the accomplishments of the EHT, which provided some deep insights into BH spacetime geometry. Particularly, the iconic depiction of a super massive BH within the M87 galaxy captured a photon ring of luminosity close to the event horizon, surrounded by an accretion disk. These observations revealed that the presence of a bright ring of radiation enclosing a central brightness depression provides the intrinsic properties of the plasma radiation near the BH. In this regard, the imaging process of BHs, the accretion of matter surrounded by high-energy radiation plays a significant role. To exhibit the results on the observer’s screen, we considered different background light sources, i.e., the spherical background light source and the thin disk accretion model. Once the simulated images are displayed on the observer’s screen, we have identified the influence of the observable properties of the celestial light source and the thin accretion disks stemming from the changes in the spacetime structure due to variation of parameters within the fabric of GK rotating BH. Particularly, this study has unveiled profound connections between parameters a , q , θ_{obs} and the optical appearance of the shadow images of spherical background light source as well as the accretion disk.

To analyze the influence of spacetime parameters, we investigated the shadow images for a nearer observer as depicted in Fig. 1. It is noticed that spin moves the shadow to the rightward of the screen and possible flatness is observed when $a = 1$, see Fig. 1 (a). On the other hand, when we varied the NED parameter q , the shadow radius decreased with the help of q as shown in Fig. 1 (b). Both parameters have the significant influence on the shadow radius as expected, which we also observed in latter discussion. By considering an observer with zero angular momentum within the domain of outer communication, the precise shape of the shadow projected on the observer screen can be obtained with the help of backward ray-tracing technique in celestial coordinates. The corresponding results interpret that the observational plane of the observer having central dark region, and outside the “D” shape petals, there is a white dashed circle. The filled dark region represents the BH shadow and white dashed circle directly demonstrated the Einstein ring, see Figs. 2-4.

Initially, we observe that NED parameter q is responsible for slightly increase the radius of Einstein ring but the size

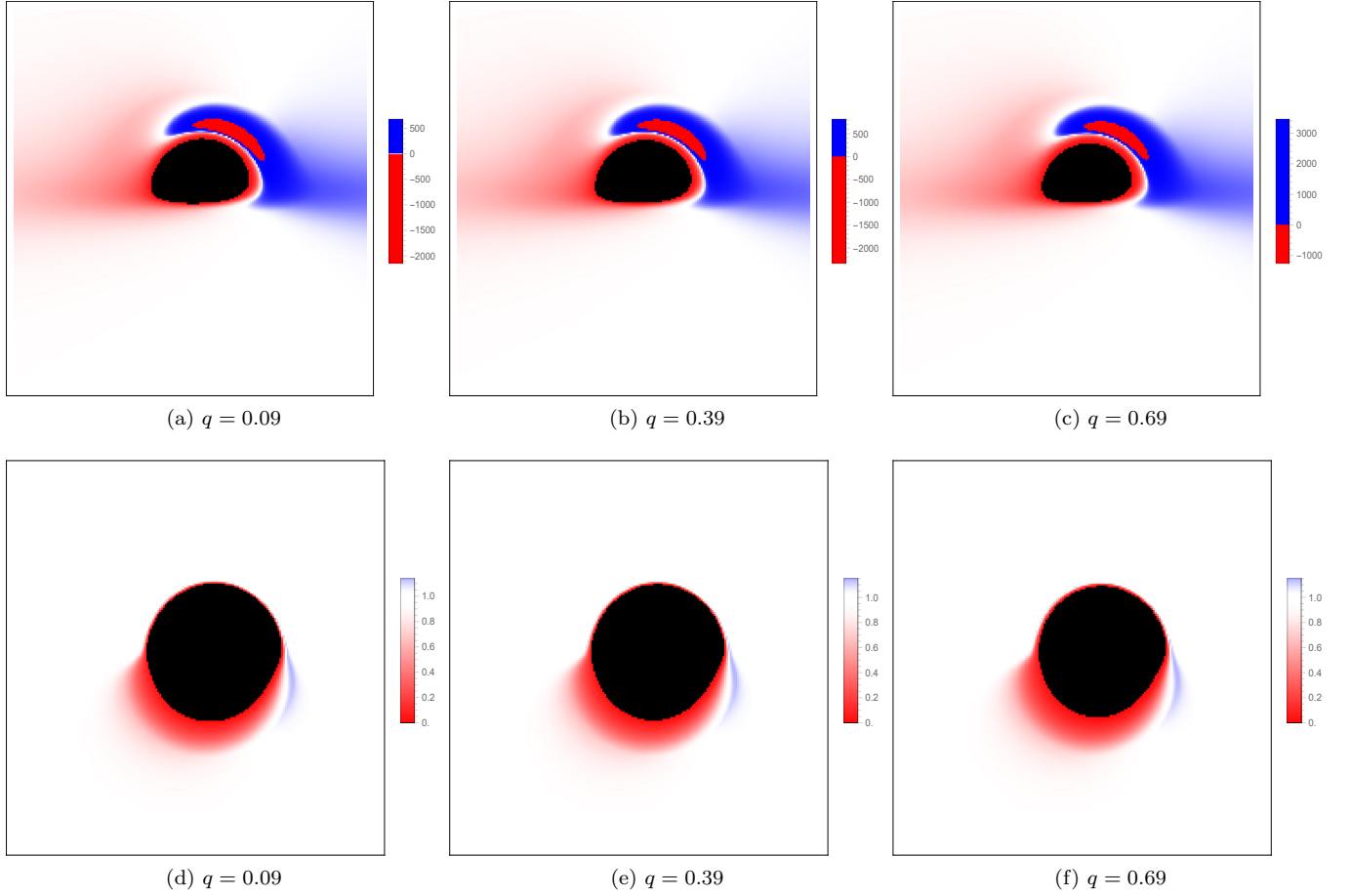


FIG. 11: The direct and lensed images of the redshift factors of the considering accretion disk model for different q are illustrated in top and bottom rows, respectively. The red and blue colors indicate the redshift and blueshift, respectively and the filled black area is the BH's event horizon. All these images portray GK rotating BHs that are illuminated by a retrograde thin equatorial accretion disk with $a = 0.69$, $\theta_{obs} = 80^\circ$, $M = 1$ and the observer's position is fixed at $r_{obs} = 500M$.

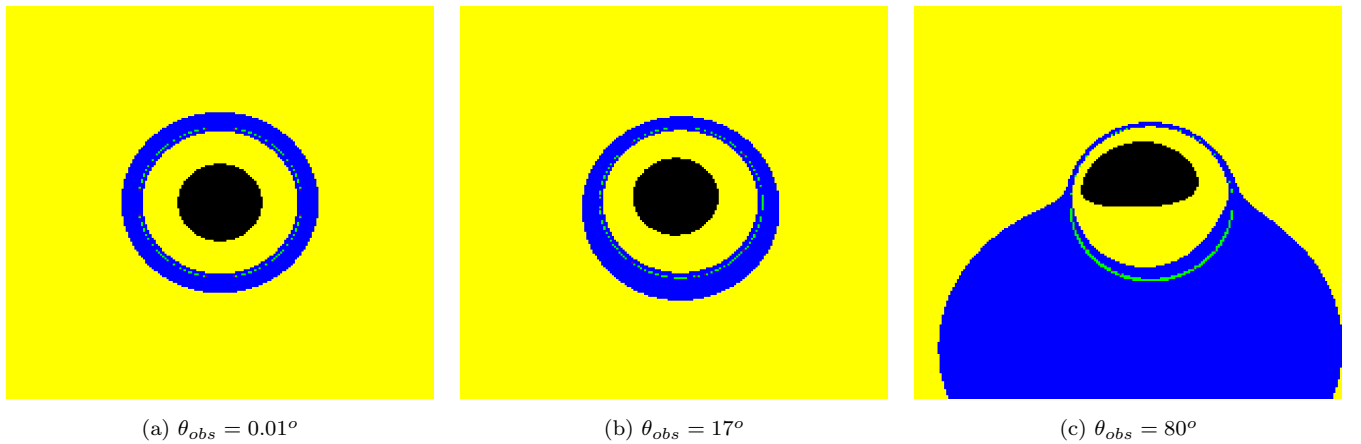


FIG. 12: The optical illustrations of direct, lensed and photons ring emissions for different inclination angle θ_{obs} . The yellow, blue and the green band colors correspond to the direct, lensed and photon ring emissions, respectively. All these images portray GK rotating BHs illuminated by a retrograde thin equatorial accretion disk with $a = 0.69$, $q = 0.39$, $M = 1$ and the observer's position is fixed at $r_{obs} = 500M$.

of the BH shadow is constant. Moreover, at $q = 1$, the resulting Einstein rings are gradually started to transform into arc-like shapes around the D-shaped configuration. When we further increase the influence of spin parameter a and vary q from left to right, the size of the BH shadow is slightly increased, and the Einstein ring shows a transition from an axisymmetric closed circle to an arc-like shape on the left and right side of the screen. These observations clearly indicate that the increasing values of a and q led to an enhancement in the degree of deformation of the shadow shape, and the optical appearance of shadow images also undergoes distortion due to the drag effect. The aforementioned details reflect the description of the Figs. 2-4, where we fixed the observation angle $\theta_{obs} = 80^\circ$. Next, we imposed a straightforward approach of spherical background light source model and analyzed the geometric details of BH images with thin accretion disk model. In the real world scenario, most of the plasma rotating around the BHs spacetime that undergoes gravitational effects and radiate high-energy particles, thereby giving rise to luminous accretion disks around the BH. Based on backward ray-tracing method, we further explored the dynamics of bright accretion disk as the fundamental source of background light source and the under consideration accretion model is assumed as an optically and geometrically thin accretion disk.

In Fig. 5, we plot the BH shadow images of thin accretion disk model for different values of q and θ_{obs} , while keeping the spin parameter a is constant. In all these images, one can always notice a filled dark region surrounded by a narrow photon ring. The dark region corresponds to accretion disk profile at $r = r_+$, so called the inner shadow while the photon ring closely aligned with the critical curve of the BH. In the first column of Fig. 5, when $\theta_{obs} = 0.01^\circ$, the dark region always lies in the center of the screen and there is a very dim strip of concentric circles appeared with the luminous ring. This will happen due to the sight line which is perpendicular to the disk and the accreting particles of the disk has no component at that sight line. This phenomenon is resulting in a little influence of Doppler effect in the redshift factor along with only gravitational redshift. When we increase the inclination angle $\theta_{obs} = 17^\circ$, as shown in the middle column of Fig. 5, one can notice that the gradual deformation in the dark central region, slightly moving towards the right bottom of the screen and there is no significant exhibition of concentric circle with the photon ring. When we further increase the value of inclination angle $\theta_{obs} = 80^\circ$, the deformation can be clearly identified where the central dark region transforms into a hat-like shape, see the right column of Fig. 5. Moreover, a prominent feature also appeared on the left side of the screen, where a luminous crescent or eyebrow-shaped region appeared which can participate to magnifies the angle, resulting in an increasingly pronounced Doppler effect. In all these cases from top to bottom, distinct features can be seen more clearly with the increase of NED parameter q . Interestingly, when θ_{obs} has smaller values, there is no significant separation between direct and lens images, because the distribution of the observed luminosity is not sharp enough. Hence, the change of observational angle does not affect the location of the critical curve, but its emission profile is slightly deformed with values of θ_{obs} . In addition, one can see the influence of NED parameter q on shadow images when we fixed $\theta_{obs} = 80^\circ$, see Fig. 6. Here, at smaller values of q , the observational luminosity of Doppler effect is relatively smaller on the left side of the screen as compared to larger one. This shows that an increase in q yields a stronger influence on the luminosity of accretion matter.

In order to analyze the realistic scenario of accreting matter around the BH, we further investigate the redshift factors of both the direct and lensed images originating from the accretion disk. Figures. 7 and 8 illustrate redshift factors for both direct and lensed images, respectively under different values of model parameters. Particularly, the top row of Fig. 7 shows that at smaller inclination angle θ_{obs} , the observer only see the redshift factors on the screen. However, with increasing θ_{obs} , one can also see the blueshift on the left side of the screen. For the middle and the bottom rows of Fig. 7, we fixed the inclination angle to $\theta_{obs} = 80^\circ$ and seen the influence of both NED and spin parameters on the redshift factors. In all these images, the observer can see both redshift and blueshift factors on the screen, but the formation of a strict red ring structure close to the inner shadow, which is attributed to the emission of light by particles within the critical plunging orbits. In Fig. 8, we demonstrated the redshift factors of the lensed images, where the parameter values correspond to those in Fig. 7. Initially, at smaller values of θ_{obs} , there is just a prominent red ring structure surrounding the inner shadow. However, when we increase $\theta_{obs} = 80^\circ$, the red color is visually represented by a continuous linear color map and on the left side of the screen, there is only a petal like map of the blue color, see the top row of Fig. 8. In the middle and the bottom rows of Fig. 8, we fixed the value of $\theta_{obs} = 80^\circ$ and varied the relevant parameters such as q and a . Here, the similar observational appearance of the redshift factors are observed as discussed in the previous case. All these results showed that the size of the inner shadow region is correlated with the values of the associated parameters, while its metamorphosis is persuaded by the observation inclination. In Fig. 9, we also plotted the direct images of the redshift factors for smaller values of q with inclination angle $\theta_{obs} = 80^\circ$ as an example. From these images, one can observe that, in addition to the influence of the magnetic field on the size of the image, there are obvious blueshift near the ISCO, and both red and blue colors are merged with each other prominently.

In Fig. 10, density profiles of BH shadow images illuminated by retrograde flows for different values of q . Here the optical appearance is suppressed with enhancing magnetic influence and morphology of the photon ring remains unaffected in all these cases. A distinct bright area resembles a crescent or an eyebrow emerges on the top right side of

the screen, where both gravitational redshift of the accretion disk are merged due to the retrograde flows. We further illustrated an investigation into the redshift of both the direct and lensed images originating from the retrograde flows in Fig. 11. It can be observed that the redshift or blueshift effect of both direct and lens images is more obvious when the parameter q has larger values. A significant difference is observed here in the case of lensed images, the effect of blueshift has appeared on the right side of the screen, which is due to retrograde flows of accretion disk, as shown in bottom panel of Fig. 11. For better understanding about the direct and lensed images of the thin accretion disk, we interpreted their observed fluxes under inclination angle θ_{obs} in Fig. 12. From these images, it can be noticed that the photon ring always lies within the range of lensed image when $\theta_{obs} = 0.01^\circ$, and showed the small amount of observed flux of the lensed emission inside the photon ring. When we increase the observed inclination angle such as $\theta_{obs} = 17^\circ$, both direct and lensed ring structures slightly deformed, and the observed flux move towards the lower half of the screen. And when $\theta_{obs} = 80^\circ$, the deformation of direct and lensed images is higher as compared to smaller values of θ_{obs} . Moreover, the majority of the observed flux of lensed emission is concentrated in the bottom half region of the screen and the central dark region is transformed into hat-like metamorphosis.

Based on our present analysis, we conclude that the above discussion may provide fruitful results for the theoretical study of the BH shadows for direct and lensed images and their relevant dynamics. Since rotating objects are considered to be more realistic in the universe, we hope that these groundbreaking results inspire the theoretical study of BH shadow images and other physical quantities that may be helpful for the observational teams working on achieving high resolution images of accretion disk.

-
- [1] K. Akiyama et al., *Astrophys. J. Lett.* **875**, L1 (2019).
 - [2] K. Akiyama et al., *Astrophys. J. Lett.* **875**, L2 (2019).
 - [3] K. Akiyama et al., *Astrophys. J. Lett.* **875**, L3 (2019).
 - [4] K. Akiyama et al., *Astrophys. J. Lett.* **875**, L4 (2019).
 - [5] K. Akiyama et al., *Astrophys. J. Lett.* **875**, L5 (2019).
 - [6] K. Akiyama et al., *Astrophys. J. Lett.* **875**, L6 (2019).
 - [7] K. Akiyama et al., *Astrophys. J. Lett.* **910**, L12 (2021).
 - [8] K. Akiyama et al., *Astrophys. J. Lett.* **910**, L13 (2021).
 - [9] K. Akiyama et al., *Astrophys. J. Lett.* **930**, L12 (2022).
 - [10] K. Akiyama et al., *Astrophys. J. Lett.* **930**, L13 (2022).
 - [11] K. Akiyama et al., *Astrophys. J. Lett.* **930**, L14 (2022).
 - [12] K. Akiyama et al., *Astrophys. J. Lett.* **930**, L15 (2022).
 - [13] K. Akiyama et al., *Astrophys. J. Lett.* **930**, L16 (2022).
 - [14] K. Akiyama et al., *Astrophys. J. Lett.* **930**, L17 (2022).
 - [15] S. E. Gralla, *Phys. Rev. D* **103**, 024023 (2021).
 - [16] F. Ozel, D. Psaltis and Z. Younsi, *Astrophys. J.* **941**, 88 (2022).
 - [17] K. Glampedakis and G. Pappas, *Phys. Rev. D* **104**, L081503 (2021).
 - [18] R. D. Blandford and R. L. Znajek, *Mon. Not. Roy. Astron. Soc.* **179**, 433 (1977).
 - [19] S. E. Gralla and A. Lupasca, *Phys. Rev. D* **101**, 044031 (2020).
 - [20] S. E. Gralla, A. Lupasca and D. P. Marrone, *Phys. Rev. D* **102**, 124004 (2022).
 - [21] S. E. Gralla, D. E. Holz, R. M. Wald, *Phys. Rev. D* **100**, 024018 (2019).
 - [22] J. P. Luminet, *Astron. Astrophys.* **75**, 228 (1979).
 - [23] K. Wu, et al., *Chin. J. Astron. Astrophys.* **6**, 205 (2006).
 - [24] K. Beckwith and C. Done, *Mon. Not. R. Astron. Soc.* **359**, 1217 (2005).
 - [25] F. H. Vincent et al., *Class. Quant. Grav.* **28**, 225011 (2011).
 - [26] M. Wang, S. Chen, J. Wang, J. Jing, *Eur. Phys. J. C* **80**, 110 (2020).
 - [27] R. Bach and H. Wevl, *Neue Lösungen der Einsteinschen Gravitationsgleichungen. B. Explizite Aufstellung statischer axialsymmetrischer Felder*, *Math. Zeit.* **13**, 134 (1922).
 - [28] R. Saleem and M. I. Aslam, *Eur. Phys. J. C* **83**, 257 (2023).
 - [29] X. X. Zeng, M. I. Aslam and R. Saleem, *Eur. Phys. J. C* **83**, 129 (2023).
 - [30] X. Y. Hu, M. I. Aslam, R. Saleem et al., *J. Cosmol. Astropart. Phys.* **2023**, 013 (2023).
 - [31] X. X. Zeng, K. J. He, J. Pu, et al., *Eur. Phys. J. C* **83**, 897 (2023).
 - [32] M. Guo, N. A. Obers and H. Yan, *Phys. Rev. D* **98**, 084063 (2018).
 - [33] X. X. Zeng, M. I. Aslam, R. Saleem et al., *Chin. Phys. C* **48**, 095108 (2024).
 - [34] M. I. Aslam, X. X. Zeng, R. Saleem et al., *Chin. Phys. C* **48**, 115101 (2024).
 - [35] X. X. Zeng, H. Q. Zhang and H. Zhang, *Eur. Phys. J. C* **80**, 872 (2020).
 - [36] X. X. Zeng and H. Q. Zhang, *Eur. Phys. J. C* **80**, 1058 (2020).
 - [37] H. Yan, M. Guo, and B. Chen, *Eur. Phys. J. C* **81**, 1 (2021).
 - [38] M. Zhang and M. Guo, *Eur. Phys. J. C* **80**, 790 (2020).
 - [39] M. Guo and P.-C. Li, *Eur. Phys. J. C* **80**, 588 (2020).

- [40] Y. Hou, M. Guo and B. Chen, Phys. Rev. D **104**, 024001 (2021).
- [41] P.-C. Li, M. Guo, and B. Chen, Phys. Rev. D **101**, 084041 (2020).
- [42] Z. Hu, Z. Zhong, P.-C. Li et al., Phys. Rev. D **103**, 044057 (2021).
- [43] C. M. Will, Living Rev. Relativ. **17**, 4 (2014).
- [44] A. De Felice and S. Tsujikawa, Phys. Lett. B **843**, 138047 (2023).
- [45] C. Lämmerzahl, M. Maceda and A. Macías, Class. Quant. Grav. **36**, 015001 (2019).
- [46] M. Born and L. Infeld, Proc. Roy. Soc. Lond. **144**, 425 (1934).
- [47] M. Demianski, Found. Phys. **16**, 187 (1986).
- [48] S. Fernando and D. Krug, Gen. Relativ. Gravit. **35**, 129 (2003).
- [49] R.-G. Cai, D.-W. Pang and A. Wang, Phys. Rev. D **70**, 124034 (2004).
- [50] E. S. Fradkin and A. A. Tseytlin, Phys. Lett. B **163**, 123 (1985).
- [51] E. Bergshoeff, E. Sezgin, C. N. Pope and P. K. Townsend, Phys. Lett. B **188**, 70 (1987).
- [52] R. R. Metsaev, M. A. Rahmanov and A. A. Tseytlin, Phys. Lett. B **193**, 207 (1987).
- [53] H. J. Mosquera Cuesta and J. M. Salim, Mon. Not. Roy. Astron. Soc. **354**, L55 (2004).
- [54] H. J. M. Cuesta and J. M. Salim, Astrophys. J. Lett. **608**, 925 (2004).
- [55] J. M. Bardeen, in Proceedings of International Conference GR5, Tbilisi, USSR (1968).
- [56] S. A. Hayward, Phys. Rev. Lett. **96**, 031103 (2006).
- [57] L. Balart and E. C. Vagenas, Phys. Lett. B **730**, 14 (2014).
- [58] L. Xiang, Y. Ling and Y. G. Shen, Int. J. Mod. Phys. D **22**, 1342016 (2013).
- [59] S. G. Ghosh and R. K. walia, Annals Phys. **434**, 168619 (2021).
- [60] R. P. Kerr, Phys. Rev. Lett. **11**, 237 (1963)
- [61] S. Vagnozzi et al., Class. Quant. Grav. **40**, 165007 (2023).
- [62] E. T. Newman, R. Couch, K. Chinnapared, A. Exton, A. Prakash and R. Torrence, J. Math. Phys. **6**, 918 (1965).
- [63] C. Bambi and L. Modesto, Phys. Lett. B **721**, 329 (2013).
- [64] E. Franzin, S. Liberati, J. Mazza and V. Vellucci, Phys. Rev. D **106**, 104060 (2022).
- [65] R. Karmakar, arXiv: 2408.11410.
- [66] L. Balart and E. C. Vagenas, Phys. Rev. D **90**, 124045 (2014).
- [67] E. T. Newman and A. I. Janis, J. Math. Phys. **6**, 915 (1965).
- [68] M. Azreg-Ainou, Phys. Rev. D **90**, 064041 (2014).
- [69] R. Shaikh, Phys. Rev. D **100**, 024028 (2019).
- [70] R. M. Wald, General Relativity (Chicago Univ. Pr., Chicago, USA, 1984).
- [71] B. Carter, Phys. Rev. **174**, 1559 (1968).
- [72] S. Chandrasekhar, The Mathematical Theory of Black Holes (Oxford University Press, Oxford, 1983). (ISBN 0-19-851291-0).
- [73] K. Meng, X.-L. Fan, S. Li et al., J. High Energy Phys. **2023**, 1 (2023).
- [74] I. Bray, Phys. Rev. D **34**, 367 (1986).
- [75] C. T. Cunningham and J. M. Bardeen, Astrophys. J. **173**, L137 (1972).
- [76] P. V. P. Cunha, C. A. R. Herdeiro, E. Radu et al., Phys. Rev. Lett. **115**, 211102 (2015),
- [77] P. V. P. Cunha, C. A. R. Herdeiro, E. Radu et al., Int. J. Mod. Phys. D **25**, 1641021 (2016), arXiv:1605.08293
- [78] F. H. Vincent, E. Gourgoulhon, C. A. R. Herdeiro et al., Phys. Rev. D **94**, 084045 (2016),
- [79] P. V. P. Cunha, J. Grover, C. A. R. Herdeiro, et al., Phys. Rev. D **94**, 104023 (2016)
- [80] J. O. Shipley, and S. R. Dolan, Class. Quantum Grav. **33**, 175001 (2016)
- [81] A. Bohn, W. Throwe, F. Hbert, K. Henriksson, and D. Bunandar, Class. Quantum Grav. **32**, 065002 (2015)
- [82] M. Wang, S. Chen and J. Jing, Phys. Rev. D **97**, 064029 (2018).
- [83] M. Wang, S. Chen and J. Jing, Phys. Rev. D **98**, 104040 (2018).
- [84] T. Johannsen, Astrophys. J. **777**, 170 (2013).
- [85] F. Long, S. Chen, M. Wang and J. Jing, Eur. Phys. J. C **80**, 1 (2020).
- [86] M. Wang, S. Chen and J. Jing, J. Cosmol. Astropart. Phys. **2017**, 051 (2017).
- [87] A. Chael, M. D. Johnson, and A. Lupsasca, Astrophys. J. **918**, 6 (2021).
- [88] R. W. Lindquist, Annals Phys. **37**, 487 (1966).
- [89] G. B. Rybicki and A. P. Lightman, *Radiative Processes in Astrophysics* (New York: Wiley-VCH) (2004).
- [90] Y. Hou, Z. Zhang, H. Yan et al., Phys. Rev. D **106**, 064058 (2022).
- [91] T. Bronzwaer and H. Falcke, Astrophys. J **920**, 155 (2021).
- [92] Z. Zhang, Y. Hou, M. Guo et al., J. Cosmol. Astropart. Phys. **2024**, 32 (2024).
- [93] C. T. Cunningham, Astrophys. J. **202**, 788 (1975).
- [94] S. Hadar, M. D. Johnson, A. Lupsasca and G. N. Wong, Phys. Rev. D **103**, 104038 (2021).